Inertial effect on dynamic hardness and apparent strain-rate sensitivity of ductile materials

Zahra Ghasemi[a], Tiago dos Santos[b], José A. Rodríguez-Martínez[c], Ankit Srivastava[a,*]

[a]*Department of Materials Science and Engineering, Texas A&M University, College Station, TX, 77843-3003, USA*
[b]*Departamento de Engenharia Mecânica, Universidade Federal de Santa Maria, Av. Roraima, 1000, Prédio 7, Santa Maria, RS, 97105-900, Brazil*
[c]*Department of Continuum Mechanics and Structural Analysis, University Carlos III of Madrid, Avda. de la Universidad, 30, 28911, Leganés, Madrid, Spain*

Abstract

Indentation is a simple and one of the oldest small-scale test methods for characterizing the mechanical response of materials. Recently, there has been a growing interest in dynamic indentation due to its potential to characterize the mechanical response of small volume of materials at high strain-rates. Herein, we focus on understanding the synergistic effects of materials' inherent strain-rate sensitivity and inertia on the scaling of dynamic hardness with indentation strain-rate. Specifically, we analyze the dynamic indentation response of ductile materials over a wide range of indentation velocities, utilizing both finite element calculations and an analytical cavity expansion model. The materials are assumed to follow isotropic elastic-viscoplastic constitutive relations, with the viscoplastic part described by either an overstress or a simple power-law model. Our results show that below a critical indentation strain-rate, the scaling of dynamic hardness with indentation strain-rate is the same as the viscoplastic constitutive description. Therefore, at these strain-rates, dynamic hardness can effectively characterize a material's strain-rate sensitivity, provided its viscoplastic constitutive description is known beforehand. However, above the critical indentation strain-rate, the dynamic hardness increases rapidly with indentation strain-rate. This phenomenon indicates an apparent strain-rate sensitivity that exceeds the expected response of the viscoplastic constitutive description. Moreover, above the critical indentation strain-rate, the indentation depth acts as a natural length-scale, with higher hardness observed at greater depths due to increased inertial effects. In other words, above the critical indentation strain-rate, dynamic hardness cannot be taken as an intrinsic material property.

Keywords: Dynamics; Indentation and hardness; Elastic-viscoplastic material; Constitutive behaviour; Finite elements; Dynamic cavity expansion

*Corresponding author: ankit.sri@tamu.edu (A. Srivastava)

1. Introduction

Characterizing the strain-rate dependent mechanical response of materials at high strain-rates is essential for a wide range of applications, including automotive and aerospace engineering, as well as for ballistic and extraterrestrial impact events (Meyers, 1994; Ramesh, 2008). Such a characterization enables enhanced safety, performance optimization, and better material selection. The range of strain-rates of interest depends on the specific application. For instance, high-speed machining typically involves strain-rates ranging from 10^2 to 10^4 s^{-1}, whereas impact loading can result in strain-rates ranging from 10^3 to 10^6 s^{-1} (Meyers, 1994). In hypervelocity extraterrestrial impact events, the strain-rates can reach as high as 10^8 s^{-1} (Ramesh, 2008). Experimental techniques for characterizing the strain-rate dependent mechanical response of materials at high strain-rates include split Hopkinson pressure bars (Hopkinson, 1914; Kolsky, 1949), Taylor impact (Taylor, 1946), plate impact (Gray, 2000), and dynamic indentation (Shore, 1907; Subhash et al., 1999), to name a few.

The dynamic indentation test is particularly appealing since it requires small volume of materials and can be used as a high-throughput test method (Liu et al., 2021; Schmalbach et al., 2021). There are two approaches to conducting dynamic indentation tests. The first approach involves impact experiments using an indenter of known geometry without directly measuring the indentation force and depth (Shore, 1907; Batson, 1918; Tabor, 1948; Davis and Hunter, 1960; Davies, 1949; Mok and Duffy, 1965; Tirupataiah and Sundararajan, 1991; Yoshioka and Yoshioka, 1995). One of the simplest methods based on this approach is conducting drop impact tests. In these tests, the rebound height or velocity change of an impacting indenter is related to the initial drop height, the impact velocity, and the volume of deformed material in the hardness impression to arrive at a "rebound hardness" (Shore, 1907). Using laser ablation techniques these tests have also been extended to micro- and nano-scales, wherein small hard particles are propelled to impact the specimen, resulting in strain-rates as high as 10^8 s^{-1} (Hassani et al., 2020). The second approach involves directly measuring the time-resolved indentation force (Crook, 1952; Nobre et al., 1997) or directly measuring both time-resolved indentation force and depth (Koeppel and Subhash, 1997; Subhash et al., 1999; Lu et al., 2003) during the dynamic indentation process. In Koeppel and Subhash (1997) and Subhash et al. (1999), the dynamic indentation test involved propelling a striker bar using a gas gun, which accelerated an incident bar with an indenter on the other end to indent the sample. The indentation force was then measured using a high-frequency piezoelectric load cell placed behind the specimen, and the indentation depth was deduced from a strain gauge mounted on the incident bar. Subsequently, Lu et al. (2003) utilized optical interferometry to more accurately measure the indentation depth. Similar concepts have been extended to characterize high strain-rate indentation force and depth response of materials at small scales using nanoindentation systems and testing techniques (Sudharshan Phani and Oliver, 2017; Guillonneau et al., 2018; Zehnder et al., 2018; Qin et al., 2019; Merle et al., 2020; Rueda-Ruiz et al., 2020; Phani et al., 2023; Hackett et al., 2023).

One way of characterizing the strain-rate dependent mechanical response of materials using dynamic indentation tests is to determine their strain-rate sensitivity exponent from

the variation of measured hardness with (a measure of) imposed strain-rate (Subhash et al., 1999; Lu et al., 2003; Sudharshan Phani and Oliver, 2017; Calle et al., 2018). However, mechanical tests do not directly measure material properties but rather the structural response, which depends on the material, specimen geometry and loading conditions. In fact, relating measured response quantities to material properties can be complex and may not always be unique, especially in indentation tests (Chen et al., 2007). Additionally, definition of several material parameters depends on the constitutive description of the material. This raises a fundamental question: Does the scaling of dynamic hardness with indentation strain-rate follow the same scaling as the strain-rate dependent (i.e., viscoplastic) constitutive description of materials? Furthermore, it has been shown that even for a material that follows strain-rate independent constitutive description, there exists a critical value of the indentation loading-rate above which the inertial effects become extremely important, leading to a rapid increase in material hardness (dos Santos et al., 2021). This raises a second question: How does the interplay of materials' strain-rate dependence and the effects of inertia affect the scaling of dynamic hardness with indentation strain-rate? These two questions are extremely important since, to the best of the authors' knowledge, all prior works assumed a simple power-law dependence of dynamic hardness on the indentation strain-rate. Additionally, none of the prior works considered the potential influence of inertia on strain-rate dependent dynamic hardness measurements.

To answer these questions, in this work, we extensively analyze dynamic indentation response of ductile materials when indented using a rigid conical indenter. The materials are assumed to follow isotropic elastic-viscoplastic constitutive relations, with the viscoplastic part described by either an overstress power-law (Cowper and Symonds, 1957) or the widely used simple power-law (Hutchinson and Neale, 1977; Needleman, 2018). We solve the dynamic indentation problem computationally using both finite element calculations and an analytical cavity expansion model. The computations are carried out for a wide range of indentation velocities. Our results show that there exists a critical indentation strain-rate below which the scaling of dynamic hardness with indentation strain-rate is the same as the viscoplastic constitutive description. Therefore, a material's strain-rate sensitivity exponent can be characterized from dynamic indentation results for a known constitutive description. However, for both viscoplastic constitutive descriptions, at any given indentation strain-rate above the critical value, the hardness depends on the indentation depth and increases rapidly compared to what is expected based on the constitutive description. In other words, at sufficiently high indentation strain-rates, the indentation depth emerges as a natural length-scale that needs to be considered when interpreting the results of dynamic indentation tests. To the best of the authors' knowledge, this paper presents the first-ever demonstration that inertia effects make dynamic hardness size-dependent. This finding emphasizes a limitation in using dynamic indentation tests to characterize the strain-rate sensitivity or strain-rate-dependent flow strength of materials at high strain-rates.

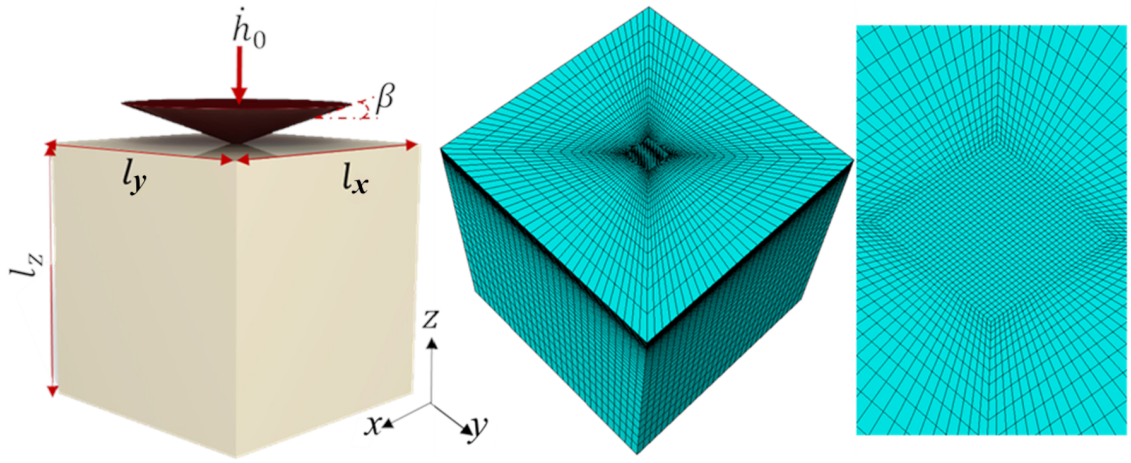

Figure 1: A schematic representation of the three-dimensional specimen being indented with a rigid conical indenter and the finite element mesh of the specimen together with a zoomed view of the same in the center of the top surface of the specimen. The dimensions of the specimen are l_x, l_y and l_z, $\dot{h}_0$ is the constant velocity imposed on the conical indenter, and $90° - \beta$ is the cone angle.

2. Finite Element Method

A series of finite element calculations of dynamic indentation of a 3D specimen with a rigid conical indenter were performed, as illustrated in Fig. 1. The specimen dimensions were set to $l_x = l_y = l_z$ =50 mm. The indenter had a tip radius of r_t =0.1 mm and cone angle of $90° - \beta$ with β =19.7°, consistent with the work of Lu et al. (2003). The finite element mesh (Fig. 1) of the specimen consisted of 140, 220 twenty-node brick elements, with a very fine uniform mesh in a 5×5×2 mm^3 region surrounding the actual indented volume.

The following displacement boundary conditions were imposed on the analyzed region: The x and y displacements of the specimen faces normal to the x and y axes, respectively, and the z displacement of the bottom face of the specimen normal to the z axis in the reference configuration were constrained. The velocity loading condition imposed on the specimen (which is initially at rest) follows the profile of the indenter penetrating the specimen and is as follows: The node at the center of the top surface of the specimen, initially in contact with the indenter tip, was given a Heaviside step velocity of $\dot{h}_0$ along the negative z axis. As deformation continued and the indenter tip penetrated the specimen, additional nodes on the top surface came into contact with the indenter. These nodes were also assigned the same z velocity, but their x and y velocities were constrained, mimicking a perfect adhesion of the material to the indenter.

The assumption of perfect adhesion between the material and the indenter is based on the work of Johnson (1970). Specifically, Johnson (1970) demonstrated that assuming the material perfectly adheres to the indenter in the finite element method results in a deformation pattern consistent with experimental evidence, i.e., the deformation occurs beneath the indenter, and the displacement fields are approximately radial. It has also been shown that for indentation using a conical indenter, perfect adhesion or frictionless conditions

between the material and the indenter have no significant effect on the resulting indentation force-depth response (Bhattacharya and Nix, 1988). The perfect adhesion condition has been utilized in a number of other works, see Fleck et al. (1992) and Danas et al. (2012), among others.

All the finite element calculations were carried out using our in-house data-parallelized finite element code (Osovski et al., 2015; N'souglo et al., 2018; Liu et al., 2019, 2020; Zheng et al., 2020). The finite element code is based on the dynamic principle of virtual work using a finite deformation Lagrangian convected coordinate formulation. Integration of internal force contributions was performed using eight-point Gaussian integration for each twenty-node element, and twenty-seven-point Gaussian integration was used for the element mass matrix. Moreover, lumped masses were used so that the mass matrix is diagonal. The discretized equations were integrated using the explicit Newmark β-method (Belytschko et al., 1976), and the constitutive behavior was updated based on the rate tangent modulus method (Peirce et al., 1984).

2.1. Constitutive Model

The material was modeled as elastic-viscoplastic, with yielding described by the von Mises criterion. Herein, the rate of deformation tensor $\boldsymbol{d}$ is represented as the sum of an elastic part $\boldsymbol{d}^e$ and a plastic part $\boldsymbol{d}^p$, i.e., $\boldsymbol{d} = \boldsymbol{d}^e + \boldsymbol{d}^p$. The elastic part is related to the Jaumann rate of the Cauchy stress tensor $\boldsymbol{\sigma}$ as

$$\hat{\boldsymbol{\sigma}} = \boldsymbol{C} : \boldsymbol{d}^e \tag{1}$$

with $\hat{()}$ denoting the objective derivative and $\boldsymbol{C}$ being the fourth rank isotropic elastic tensor

$$\boldsymbol{C} = \frac{E}{1+\nu}\boldsymbol{I}' + \frac{E}{3\left(1-2\nu\right)}\mathbf{1} \otimes \mathbf{1} \tag{2}$$

where E is the Young's modulus, ν is the Poisson's ratio, $\boldsymbol{I}'$ is the unit-deviatoric fourth rank tensor, and $\mathbf{1}$ is the unit second rank tensor.

The plastic part of the rate of deformation tensor is given as

$$\boldsymbol{d}^p = \dot{\lambda}\frac{\partial \Phi}{\partial \boldsymbol{\sigma}} \tag{3}$$

where $\dot{\lambda}$ is a non-negative plastic multiplier rate and

$$\Phi = \frac{\bar{\sigma}}{\sigma_Y} - 1 \leqslant 0 \tag{4}$$

is the von Mises flow potential, where $\bar{\sigma} = \sqrt{\frac{3}{2}\boldsymbol{s} : \boldsymbol{s}}$ is the von Mises effective stress with $\boldsymbol{s} = \boldsymbol{\sigma} - \frac{1}{3}\left(\boldsymbol{\sigma} : \mathbf{1}\right)\mathbf{1}$, and

$$\sigma_Y = \sigma_0 \left(1 + \frac{\bar{\varepsilon}^p}{\varepsilon_0}\right)^n \left[1 + \left(\frac{\dot{\bar{\varepsilon}}^p}{\dot{\varepsilon}_0}\right)^m\right] G\left(T\right) \tag{5}$$

is the yield stress, where $\dot{\bar{\varepsilon}}^p = \sqrt{\frac{2}{3}\boldsymbol{d}^p : \boldsymbol{d}^p}$ is the equivalent plastic strain-rate, $\bar{\varepsilon}^p = \int_0^t \dot{\bar{\varepsilon}}^p(\tau)\, d\tau$ is the accumulated equivalent plastic strain, and T is the current temperature; while σ_0 is the reference yield strength, n is the strain hardening exponent, ε_0 is a reference strain, m is the strain-rate sensitivity (or hardening) exponent, and $\dot{\varepsilon}_0$ is a reference stain rate. The dependence of σ_Y on $\dot{\bar{\varepsilon}}^p$ in Eq. (5) is referred to as the overstress power-law (Cowper and Symonds, 1957).

The temperature dependence of σ_Y in Eq. (5) is taken as

$$G(T) = 1 + b\exp\left(-c\left[T_0 - 273\right]\right)\left[\exp\left(-c\left[T - T_0\right]\right) - 1\right] \tag{6}$$

where b and c are constitutive parameters and T_0 is a reference temperature.

Assuming adiabatic deformation process (no heat flux), and considering that plastic work is the only source of heating, the temperature evolution is given as

$$\dot{T} = \chi \frac{\bar{\sigma}\dot{\bar{\varepsilon}}^p}{\rho C_p} \tag{7}$$

where χ is the Taylor-Quinney coefficient, C_p is the specific heat, and $\rho = \rho_0/\det(\boldsymbol{F})$ is the current material density, with ρ_0 being the initial material density and $\boldsymbol{F}$ the deformation gradient tensor.

Finally, from the equivalence of macroscopic plastic work and microscopic plastic dissipation i.e., $\boldsymbol{\sigma} : \boldsymbol{d}^p = \bar{\sigma}\dot{\bar{\varepsilon}}^p$, we get $\dot{\lambda} = \dot{\bar{\varepsilon}}^p$ in Eq. (3).

2.2. Constitutive Model Calibration

The constitutive model described in Section 2.1 contains various parameters that need to be determined for a given material. In this work, we focused on OFHC copper as a model material since it has been extensively characterized using a variety of techniques. Additionally, this choice is consistent with the dynamic indentation experiments in Lu et al. (2003). As such the elastic constants were taken to be $E = 116$ GPa and $\nu = 0.31$, the initial density was set to $\rho_0 = 8940$ kg/m^3, and the specific heat was set to $C_p = 384.6$ J/kg-K. The Taylor-Quinney coefficient was assumed to be $\chi = 0.9$. The values of the remaining parameters, i.e., those in Eqs. (5) and (6), were determined using the experimental results of mechanical testing of OFHC copper found in the literature (Tong et al., 1992; Tanner and McDowell, 1999; Rittel et al., 2002). In these works, the quasi-static mechanical testing was performed using servo-hydraulic machines, while dynamic mechanical testing was conducted using a Kolsky bar and pressure-shear plate impact tests. These tests quantified the material's stress-strain response (Tong et al., 1992) and the relationship between flow stress and the imposed strain-rate (Tong et al., 1992; Rittel et al., 2002) and test temperature (Tanner and McDowell, 1999), as illustrated in Fig. 2. From these experimental results, the values of the parameters in Eq. (5) were found to be $\sigma_0 = 302$ MPa, $n = 0.21$, $\varepsilon_0 = 0.44$, $m = 0.35$, and $\dot{\varepsilon}_0 = 2.2 \cdot 10^4$ s^{-1}, and those in Eq. (6) were found to be $b = 5.71$ and $c = 3.52 \cdot 10^{-4}$ with $T_0 = 293$ K. Note that 293 K is also the initial temperature in all calculations, meaning $T = T_0$ at $t = 0$. The comparison of the experimental and predicted mechanical response of the material using these values of the constitutive parameters is

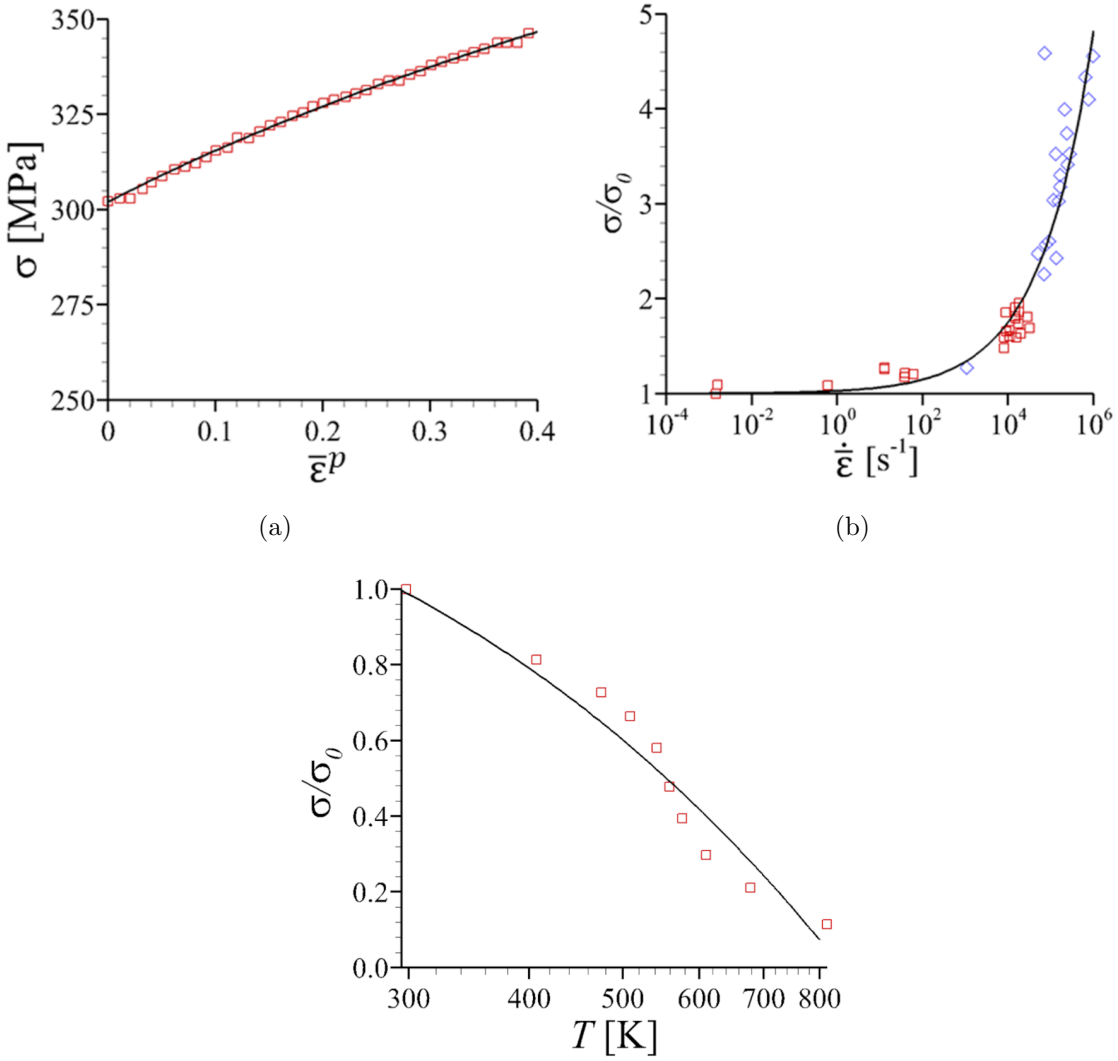

Figure 2: Comparison of the mechanical response of an OFHC copper obtained experimentally (symbols) and predicted (solid line) using the calibrated constitutive model with overstress power-law description for the strain-rate dependence. (a) Quasi-static true stress (σ) - effective plastic strain ($\bar{\varepsilon}^p$) response. (b) The dependence of the normalized flow stress (σ/σ_0) on the imposed nominal effective strain-rate ($\dot{\bar{\varepsilon}}$). (c) The dependence of σ/σ_0 on temperature (T). The experimental data in (a) are from Tanner and McDowell (1999). The experimental data in (b), square and diamond symbols, are from Rittel et al. (2002) and Tong et al. (1992), respectively. The experimental data in (c) are from Tanner and McDowell (1999). In (b) and (c), $\sigma_0 = 302$ MPa. The horizontal axis in (b) is on the log scale.

shown in Fig. 2. We note that the dynamic indentation test results of Lu et al. (2003) are not utilized for the calibration of the constitutive model. Instead, in this paper, these dynamic indentation test results are solely employed to validate the finite element predictions.

3. Finite Element Results

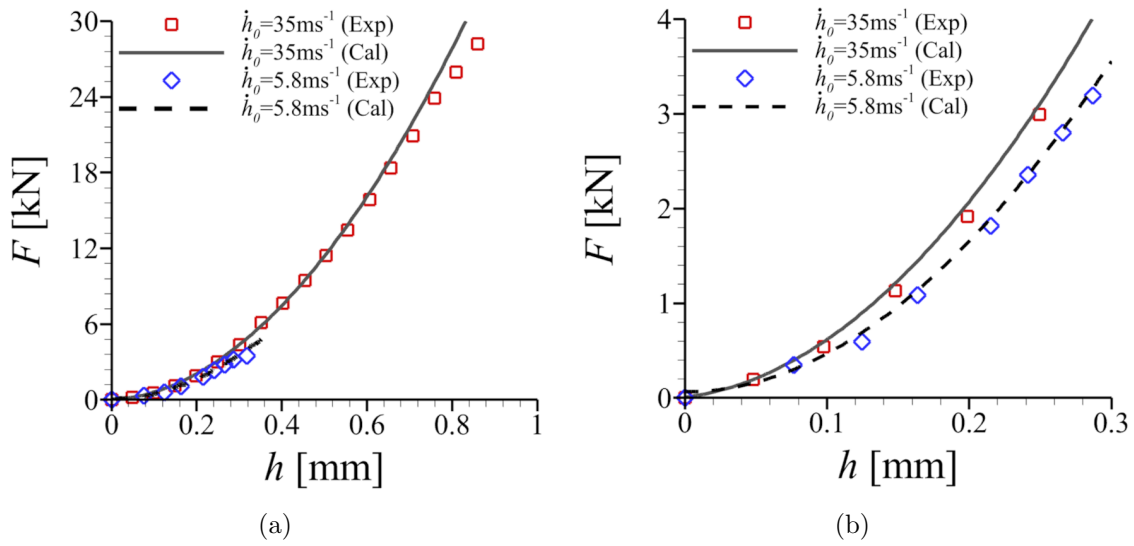

Figure 3: (a) Comparison of the experimentally (Exp) obtained and calculated (Cal) indentation force (F) - depth (h) response for two values of the imposed indentation velocity ($\dot{h}_0$). (b) The zoomed-in view of the plot in (a) showing the comparison of the experimental and calculated F - h response at lower indentation depths. The finite element calculations were carried out using the calibrated constitutive model with overstress power-law description for the strain-rate dependence. The experimental data are taken from Lu et al. (2003).

A comparison of the indentation force (F) - depth (h) response for two values of the imposed indentation velocity ($\dot{h}_0$) predicted using the fully calibrated overstress power law constitutive model and the experimental results of Lu et al. (2003) is shown in Fig. 3. An excellent quantitative agreement between the predicted and experimentally measured $F-h$ response for the full range of the values of h is noted from Figs. 3(a) and (b). As discussed in Section 2.2, we calibrated the constitutive model using the results of quasi-static uniaxial mechanical tests and dynamic mechanical tests involving Kolsky bar and pressure-shear plate impact tests (Tong et al., 1992; Tanner and McDowell, 1999; Rittel et al., 2002), and not the dynamic indentation test results of Lu et al. (2003). This is because even though the indentation response of a material using a conical indenter may not be unique (Chen et al., 2007), meaning a wide range of constitutive parameter values can lead to the same indentation response, the indentation response of a fully calibrated constitutive model is unique. The experimental work of Lu et al. (2003) represents a significant milestone in the area of dynamic indentation testing and is one of the few works that reported full indentation force - depth response. The observed quantitative agreement between our predictions and their experimental results provides robust validation of our computational approach and instills confidence in the numerical predictions presented hereafter.

The indentation $F-h$ response of the material for a fixed value of the imposed $\dot{h}_0$ is

used to estimate the material's hardness (H) and the nominal indentation strain-rate ($\dot{\bar{\varepsilon}}_i$) as

$$H = \frac{F(h)}{A(h)}; \qquad \dot{\bar{\varepsilon}}_i = \frac{\dot{h}_0}{h} \tag{8}$$

where $A(h)$ is the cross sectional area of the conical indenter in contact with the material at an indentation depth h. The definition of $\dot{\bar{\varepsilon}}_i$ follows from the work of Subhash et al. (1999).

Next, to answer the question of whether the scaling of H with $\dot{\bar{\varepsilon}}_i$ follows the same scaling as the strain-rate dependent constitutive description of the material, we also repeated all the dynamic indentation finite element calculations with a simple power-law description of the strain-rate dependence in Eq. (5). The simple power-law based description of the strain-rate dependence is given as (Hutchinson and Neale, 1977; Needleman, 2018)

$$\sigma_Y = \sigma_0 \left(1 + \frac{\bar{\varepsilon}^p}{\varepsilon_0}\right)^n \left(\frac{\dot{\bar{\varepsilon}}^p}{\dot{\varepsilon}_0}\right)^m G\left(T\right) \tag{9}$$

The values of the constitutive parameters for the simple power-law in Eq. (9) are also taken to be the same as for the overstress power-law in Eq. (5) and reported in Section 2.2. For both descriptions of the strain-rate dependence of the material, finite element calculations of dynamic indentation are carried out for twenty two values of $\dot{h}_0$ ranging from 0.3 m/s to 158 m/s.

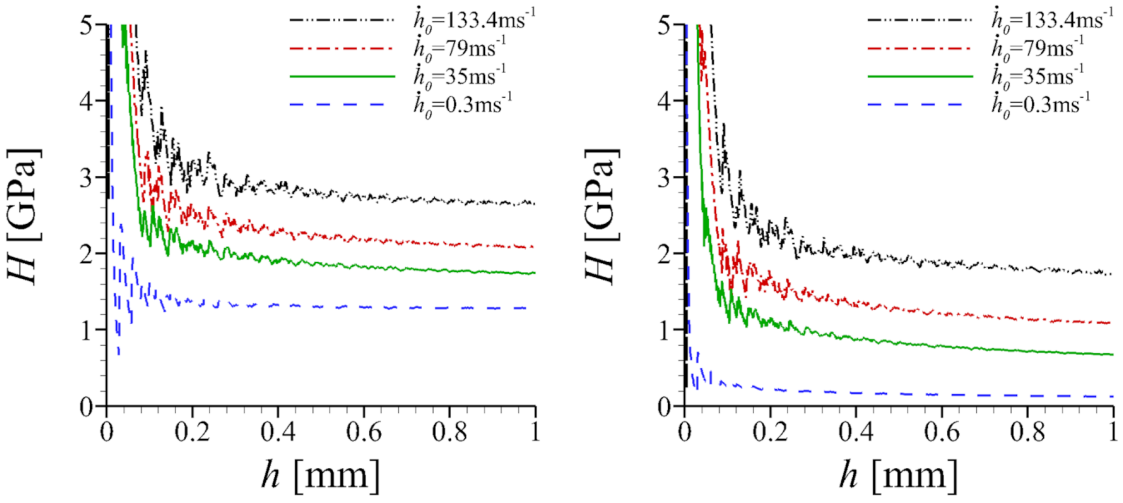

Figure 4: Variation of hardness (H) with indentation depth (h) for four values of the imposed indentation velocity ($\dot{h}_0$) obtained from the finite element calculations. (a) For calculations using the overstress power-law description for the strain-rate dependence. (b) For calculations using the simple power-law description for the strain-rate dependence.

Figure 4 shows the evolution of H as a function of h for four values of $\dot{h}_0$. The results obtained with overstress and simple power-law descriptions of strain-rate dependence of the

material are shown in subfigures (a) and (b), respectively. As shown in the figure, at the start of the indentation process, the value of H is unbounded because $A(h)$ is infinitesimally small. Additionally, since the specimen is initially at rest and the imposed indentation loading condition is a Heaviside step velocity, the value of $\dot{\bar{\varepsilon}}_i$ is extremely large in the beginning, and the sudden acceleration of the specimen leads to oscillations in the $H-h$ curves for $h < 0.2$. These oscillations do decay gradually with increasing h. As the value of h increases, the value of $A(h)$ also increases while that of $\dot{\bar{\varepsilon}}_i$ decreases, resulting in a rapid decrease in the value of H. For $h > 0.2$, the value of H tends to decrease gradually with a continued increase in h. This is because the value of $\dot{\bar{\varepsilon}}_i$ is not constant for a fixed value of the imposed $\dot{h}_0$, and it depends on the value of h, see Eq. (8). Thus, even for a constant $\dot{h}_0$, the value of H depends on the value of h. The $H-h$ curves for all values of $\dot{h}_0$ are qualitatively similar for both viscoplastic constitutive models. For both models, an increase in the value of $\dot{h}_0$ for a given value of h results in an increase in the value of H due to the associated strain-rate hardening and inertia. However, at any given value of h and for a fixed value of $\dot{h}_0$, the overstress power-law model exhibits a greater value of H compared to the simple power-law model. This is due to the fact that the flow strength of the material with the same set of constitutive parameters, but governed by the overstress power-law model, is greater than that of the material governed by the simple power-law model for the same imposed strain-rate, see Eqs. (5) and (9).

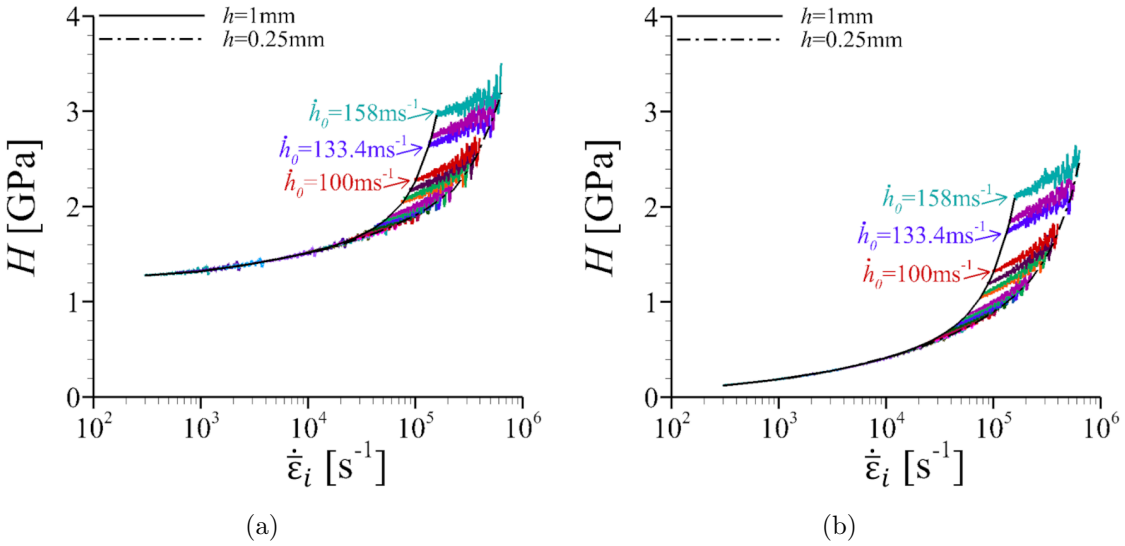

Figure 5: Variation of hardness (H) with nominal indentation strain-rate ($\dot{\bar{\varepsilon}}_i$) obtained from the finite element calculations for the values of the imposed indentation velocity ($\dot{h}_0$) ranging from 0.3 m/s to 158 m/s and for the values of the indentation depth (h) ranging from 0.25 mm to 1 mm. (a) For calculations using the overstress power-law description for the strain-rate dependence. (b) For calculations using the simple power-law description for the strain-rate dependence. The horizontal axis in both (a) and (b) are on the log scale.

The evolution of H as a function of $\dot{\bar{\varepsilon}}_i$ for the values of $\dot{h}_0$ ranging from 0.3 m/s to 158

m/s is shown in Fig. 5. Here as well, the results obtained with overstress and simple power-law models are shown in subfigures (a) and (b), respectively. In Fig. 5, the evolution of H with $\dot{\bar{\varepsilon}}_i$ is plotted for $h \in [0.25, 1]$ mm with different colors for all values of $\dot{h}_0$ considered in this work. Additionally, the variation of the value of H with $\dot{\bar{\varepsilon}}_i$ is also shown for $h = 0.25$ mm and 1 mm to illustrate the bounds. The range of values of $\dot{\bar{\varepsilon}}_i$ shown in Fig. 5 spans from relatively low values that are consistent with the works of Subhash et al. (1999) and Lu et al. (2003) to high values that are consistent with the works of Tirupataiah and Sundararajan (1991) and Hassani et al. (2020).

However, these prior works did not address the two fundamental questions posed in this work: Does the scaling of dynamic hardness with indentation strain-rate follow the same scaling as the strain-rate dependent constitutive description of materials? and how does the interplay of the materials' strain-rate dependence and the effects of inertia affect the scaling of dynamic hardness with indentation strain-rate? It is also worth noting that Tirupataiah and Sundararajan (1991) hypothesized that the inertial resistance of the target material should be negligible compared to its resistance to plastic flow for the interpretation of dynamic hardness measurements to be considered valid. Answering the two aforementioned fundamental questions will provide verification and rationale for this three-decades-old hypothesis. While Lu et al. (2003) performed finite element analyses of dynamic indentation, their focus was solely on comparing the experimentally and computationally obtained variations of a measure of flow strength of the material with a measure of strain-rate. Both the flow strength and strain rate in their work were empirically deduced from the dynamic indentation results. Thus, the existing literature has left these two critical questions largely unexplored, and addressing them is a central focus of the results presented hereafter.

As shown in Fig. 5, both overstress and simple power-law models produce qualitatively similar $H - \dot{\bar{\varepsilon}}_i$ responses, but for a fixed value of $\dot{\bar{\varepsilon}}_i$, the overstress power-law model yields higher values of H compared to the simple power-law model. This is because the flow strength of the material governed by the overstress power-law model is greater than that of the material governed by the simple power-law model for the same imposed strain-rate, as noted earlier. Nonetheless, while the value of H remains finite for the overstress power-law model at all values of $\dot{\bar{\varepsilon}}_i$, see Fig. 5(a), the value of H for the simple power-law model tends to zero, see Fig. 5(b), as the value of $\dot{\bar{\varepsilon}}_i$ decreases. This is due to the fact that the flow strength of the material governed by the overstress power-law model tends to a reference value as the imposed strain-rate tends to zero while that of the material governed by the simple power-law model tends to zero, see Eqs. (5) and (9).

The results in Fig. 5 demonstrate that, for both viscoplastic constitutive models and indentation depths in the range of 0.25 to 1 mm, the value of H is independent of h and increases with an increasing value of $\dot{\bar{\varepsilon}}_i$ for $\dot{\bar{\varepsilon}}_i < 5 \times 10^4$ s^{-1}. This finding implies that the value of H for $\dot{\bar{\varepsilon}}_i < 5 \times 10^4$ s^{-1} is solely determined by the nominal strain-rate, and as such, is a material property directly linked to the strain-rate dependent flow strength of the material. In contrast, for $\dot{\bar{\varepsilon}}_i > 5 \times 10^4$ s^{-1} (referred to hereafter as the critical indentation strain-rate), the evolution of H with $\dot{\bar{\varepsilon}}_i$ becomes dependent on the value of h and increases rather rapidly with further increases in $\dot{\bar{\varepsilon}}_i$. Importantly, for a given value of $\dot{\bar{\varepsilon}}_i > 5 \times 10^4$ s^{-1}, the dependence of H on h is such that the value of H increases with increasing value

of h, indicating that it can no longer be treated as a material property. The h-dependent evolution of H above a critical indentation strain-rate is due to inertial effects since the constitutive models do not have any explicit length-scale. Nonetheless, this behavior is physically sound because for a given indentation strain-rate, a greater depth of indentation requires more material to be displaced, resulting in an increase in the inertial effect and the hardness of the material. This is the first-ever demonstration that inertia effects make dynamic hardness measurements size-dependent, even in the absence of any length-scale in the constitutive model.

The value of the critical indentation strain-rate, $\approx 5 \times 10^4$ s^{-1}, identified for h values ranging from 0.25 to 1 mm for both viscoplastic constitutive models, above which inertial effects become increasingly significant, is not likely to be universal and will depend on various other parameters. These parameters will include both material and geometrical factors, such as material density and indenter shape.

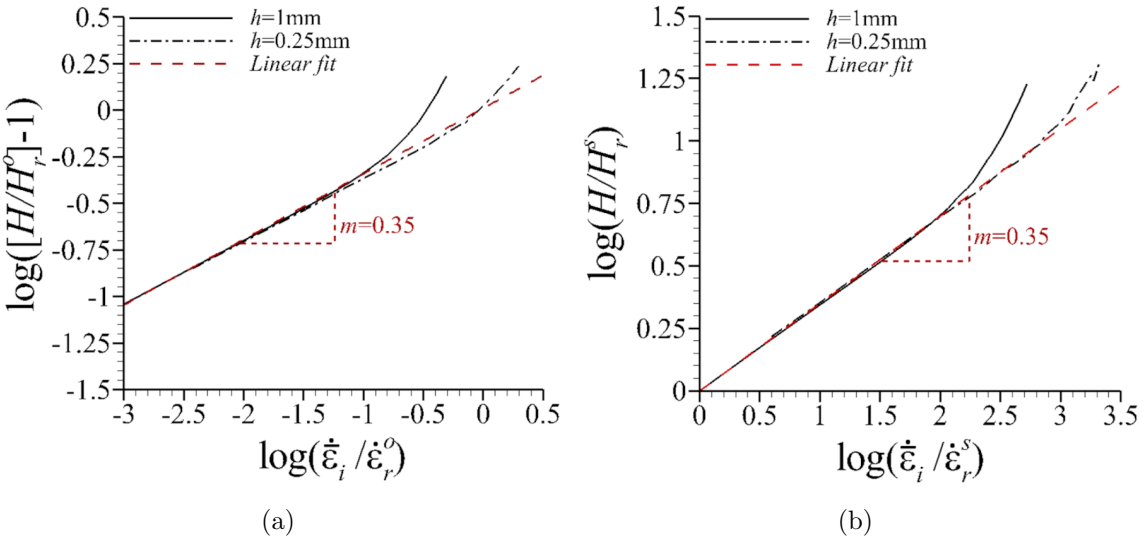

(a) (b)

Figure 6: Graphical representation of (a) Eq. (10) corresponding to the overstress power-law model and (b) Eq. (11) corresponding to the simple power-law model showing the dependence of hardness (H) on the nominal indentation strain-rate ($\dot{\bar{\varepsilon}}_i$) at two values of the indentation depth (h) and for the range of indentation velocity ($\dot{h}_0$) considered. The normalization parameters H_r^o and $\dot{\varepsilon}_r^o$ in (a) are fitting constants, while H_r^s and $\dot{\varepsilon}_r^s$ in (b) are the values of the hardness and indentation strain-rate, respectively, corresponding to the lowest value of the indentation velocity considered herein. The parameter m in (a) and (b) is the slope of the linear portion of the curve.

In Fig. 6, we attempt to quantify the scaling of H with $\dot{\bar{\varepsilon}}_i$ and check to what extent it follows the same scaling as the strain-rate dependent constitutive description of the material. To this end, we assume that the increase in H with increasing $\dot{\bar{\varepsilon}}_i$ is a result of the strain-rate sensitivity of the material as described by the constitutive models in Eqs. (5) and (9). To quantify this relationship, we derive analogous expressions for the dependence of H on $\dot{\bar{\varepsilon}}_i$ as follows

$$\log\left(\frac{H}{H_r^o}-1\right)=m\log\left(\frac{\dot{\bar{\varepsilon}}_i}{\dot{\varepsilon}_r^o}\right) \tag{10}$$

for the overstress power-law description for the strain-rate dependence and

$$\log\left(\frac{H}{H_r^s}\right)=m\log\left(\frac{\dot{\bar{\varepsilon}}_i}{\dot{\varepsilon}_r^s}\right) \tag{11}$$

for the simple power-law description of the strain-rate dependence of the material.

Figures 6(a) and (b) show the plots of Eqs. (10) and (11), respectively. The parameters $H_r^o = 1.17$ GPa, $\dot{\varepsilon}_r^o = 3.17 \times 10^5$ s^{-1}, and $m = 0.35$ in Eq. (10) are identified by fitting the equation to the H versus $\dot{\bar{\varepsilon}}_i$ data for $\dot{\bar{\varepsilon}}_i < 10^4$ s^{-1} obtained from the finite element calculations using overstress power-law model. In Eq. (11), for the simple power-law model, the values of the parameters $H_r^s = 0.125$ GPa, $\dot{\varepsilon}_r^s = 3 \times 10^2$ s^{-1}, and $m = 0.35$. The values of H_r^s and $\dot{\varepsilon}_r^s$ are simply the values of H and $\dot{\bar{\varepsilon}}_i$ at $h = 1$ mm for $\dot{h}_0 = 0.3$ m/s , which is the lowest value of the indentation velocity considered in this work, while the value of m is identified by fitting the equation to the H versus $\dot{\bar{\varepsilon}}_i$ data for $\dot{\bar{\varepsilon}}_i < 10^4$ s^{-1} obtained from the finite element calculations using simple power-law model. Of particular importance is the fact that the slopes (m) of the linear portion of the log-log plots in Figs. 6(a) and (b) are the same as the strain-rate sensitivity exponents used in the finite element calculations only if the hardness vs. indentation strain-rate data are analyzed using a relation consistent with the underlying viscoplastic constitutive description of the material. In other words, if the data in Fig. 6(a) were analyzed as per Eq. (11), the resultant slope is not the same as the strain-rate sensitivity exponents used in the finite element calculations. Furthermore, analyzing the data beyond the linear portion of the log-log plots in Figs. 6(a) and (b) will yield a value of m that is greater than the actual strain-rate sensitivity exponent of the material. Beyond the linear portion, the scaling of H with $\dot{\bar{\varepsilon}}_i$ no longer follows the same trend as expected based on materials' strain-rate dependent constitutive description, confirming that dynamic hardness is no longer an intrinsic material property.

The increase in dynamic hardness beyond the strain-rate hardening of the material is attributed to the development of large hydrostatic stresses induced by inertia in the specimen as the indentation velocity increases. Contour plots of the variation of hydrostatic stress around the indenter at an indentation depth of $h = 1$ mm for two values of the imposed indentation velocity, $\dot{h}_0 = 0.96$ m/s and 100 m/s, are shown in Fig. 7. In the figure, the results are shown for both overstress and simple power-law models. As can be seen in the figure, both constitutive models yield similar qualitative results, showing the formation of a hemispherical core below the indenter tip with large hydrostatic stress. The difference in results obtained for the two constitutive models is quantitative in nature. Specifically, the hydrostatic stress in the hemispherical core is lower for the simple power-law model compared to the overstress power-law model, because the flow strength of the former is less than that of the latter at the same imposed strain-rate. However, as the indentation velocity increases

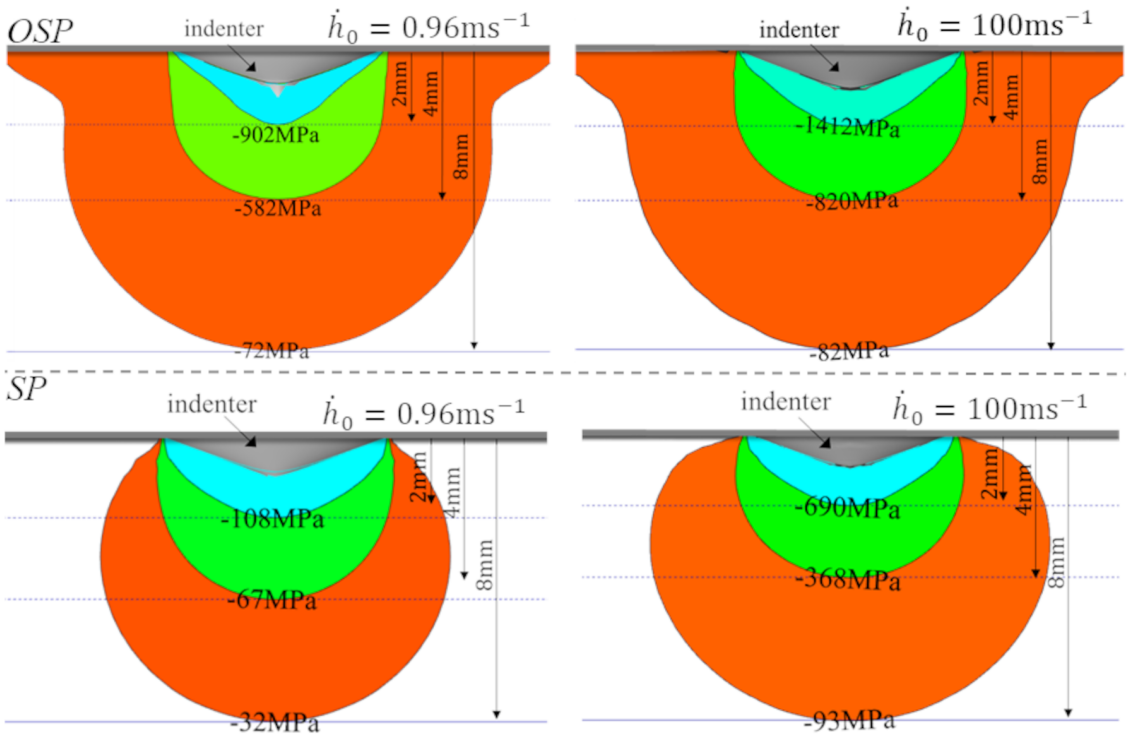

Figure 7: Contour plots showing the variation of hydrostatic stress around the indenter at an indentation depth of $h = 1$ mm for two values of the imposed indentation velocity, $\dot{h}_0 = 0.96$ m/s and 100 m/s (corresponding to $\dot{\varepsilon}_i = 960\ \text{s}^{-1}$ and $10^5\ \text{s}^{-1}$), obtained from finite element calculations using both overstress power-law (OSP) and simple power-law (SP) descriptions for the strain-rate dependence.

from $\dot{h}_0 = 0.96$ m/s to 100 m/s, the inertial effects dominate, and the increase in hydrostatic stress is significantly greater than the expected increase due to the strain-rate-dependent enhancement of the material's flow strength. Nonetheless, the increase in hydrostatic stress is relatively similar for both models as the indentation velocity increases. For example, at a depth of 1 mm below the indenter tip (i.e., 2 mm below the specimen surface), the increase in hydrostatic stress is 510 MPa and 582 MPa for the overstress and simple power-law models, respectively. Similarly, at a depth of 3 mm below the indenter tip, the increase in hydrostatic stress is 238 MPa and 301 MPa for the overstress and simple power-law models, respectively.

4. Analytical Model

The dynamic cavity expansion model utilized in this paper adapts the viscoplastic formulation of dos Santos et al. (2020) to the constitutive framework introduced in Section 2.1, and the process of conical indentation is idealized as the radial expansion of a spherical cavity into an infinite medium (Johnson, 1970; Studman et al., 1977; Fleck et al., 1992; Gao et al., 2006; Mata et al., 2006). The cavity expansion model assumes that the indenter is encased in a rigid hemispherical core of radius a (the expanding cavity) that is subject to

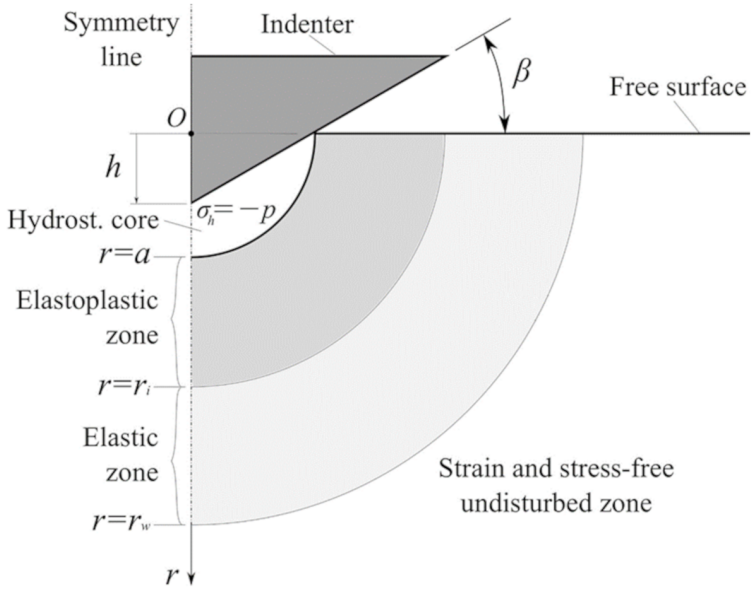

Figure 8: A schematic illustrating the idealization of the indentation process using a conical indenter as the radial expansion of a spherical cavity.

a hydrostatic stress equal to the indentation pressure p, which corresponds to the specimen hardness, as shown in Fig. 8. Note that the assumption of a hydrostatic core developing below the indenter tip is consistent with the finite element results presented in Fig. 7.

We consider an Eulerian spherical coordinate system (r, θ, ϕ) with the origin located at the center of the hydrostatic core. The indenter penetrates the solid at a constant velocity $\dot{h}$, such that a steady-state indentation pressure is achieved, causing the material to displace radially at velocity $\dot{r}$. We assume that all field variables depend on the normalized radial coordinate $\xi = r/a$ (Durban and Masri, 2004; Masri and Durban, 2005; Cohen and Durban, 2013b), which allows us to transform the field equations (i.e., balance of linear momentum, constitutive relations, heat equation, and conservation of mass) to obtain the following set of expressions:

$$\Sigma'_{rr} + \frac{2}{\xi}\left(\Sigma_{rr} - \Sigma_{\theta\theta}\right) = M^2 \frac{\rho}{\rho_0}\left(V - \xi\right) V' \tag{12}$$

$$V' = \left(V - \xi\right)\left[\Sigma'_{rr} - 2\nu\Sigma'_{\theta\theta} - \left(\bar{\varepsilon}^p\right)'\right] \tag{13}$$

$$\frac{V}{\xi} = \left(V - \xi\right)\left[-\nu\Sigma'_{rr} + \left(1 - \nu\right)\Sigma'_{\theta\theta} + \frac{1}{2}\left(\bar{\varepsilon}^p\right)'\right] \tag{14}$$

$$\left(\bar{\varepsilon}^p\right)' = \frac{a}{\dot{a}\left(V - \xi\right)}\dot{\varepsilon}_0 \left[\frac{\Sigma_{\theta\theta} - \Sigma_{rr}}{\Sigma_0\left(1 + \frac{\bar{\varepsilon}^p}{\varepsilon_0}\right)^n G\left(T\right)} - 1\right]^{\frac{1}{m}} \tag{15}$$

$$\frac{\rho C_p}{E} T' = \chi \bar{\Sigma} \left(\bar{\varepsilon}^p\right)' \tag{16}$$

$$\frac{\rho}{\rho_0} = \exp\left[-(1-2\nu)(\Sigma_{rr} + 2\Sigma_{\theta\theta})\right] \tag{17}$$

which have been normalized using the following dimensionless groups:

$$\Sigma_{rr} = \frac{\sigma_{rr}}{E}; \qquad \Sigma_{\theta\theta} = \frac{\sigma_{\theta\theta}}{E}; \qquad \Sigma_0 = \frac{\sigma_0}{E}; \qquad \bar{\Sigma} = \frac{\bar{\sigma}}{E}$$

$$P = \frac{p}{E}; \qquad M = \frac{\dot{a}}{\sqrt{\frac{E}{\rho_0}}}; \qquad V = \frac{\dot{r}}{\dot{a}}$$

with the prime superscript denoting differentiation with respect to ξ.

The Eq. (15) is obtained with the overstress power-law description of the strain-rate dependence, see Eq. (5), so that considering the simple power-law in the cavity expansion model requires using Eq. (9) to compute $(\bar{\varepsilon}^p)'$. Moreover, the strain-rate sensitivity of the material makes the dynamic cavity expansion model to be time-dependent, so that it is required to specify the time t at which the corresponding cavitation field is evaluated (dos Santos et al., 2020). For a constant-velocity expansion, the current hydrostatic core radius is calculated as $a = a_0 + \dot{a}t$, where a_0 is the hydrostatic core radius at $t = 0$ (hydrostatic core radius at a reference time).

The set of Eqs. (12)-(17) is solved using an iterative shooting method under the following boundary conditions

$$V = \frac{\tan\beta}{2} \quad \text{and} \quad \Sigma_{rr} = -P, \quad \text{at} \quad \xi = 1$$

$$V = 0, \quad \Sigma_{rr} = \Sigma_{\theta\theta} = 0, \quad \text{at} \quad \xi = \xi_w$$

to obtain the values of six unknowns $(V, \Sigma_{rr}, \Sigma_{\theta\theta}, \bar{\varepsilon}^p, T, \rho)$, and the calculated radial stress at the cavity boundary provides the specimen hardness. The reader is referred to dos Santos et al. (2020, 2021), Cohen et al. (2010) and Cohen and Durban (2013a) for more details on the derivation of the dynamic cavity expansion model.

5. Analytical Model Results and Discussion

The analytical model predictions for the variation of hardness (H) with indentation strain-rate ($\dot{\bar{\varepsilon}}_i$) using the two viscoplastic constitutive descriptions, overstress and simple power-law, are shown in Figs. 9(a) and (b), respectively. The results are obtained for two values of the indentation depth, $h = 1$ mm and 0.25 mm, and for a wide range of values of the imposed indentation velocity ($\dot{h}_0$). To facilitate direct comparison with the analytical model predictions, the finite element results shown in Fig. 5 are also reproduced in Fig. 9. As the overstress power-law constitutive model was calibrated for OFHC copper, limited

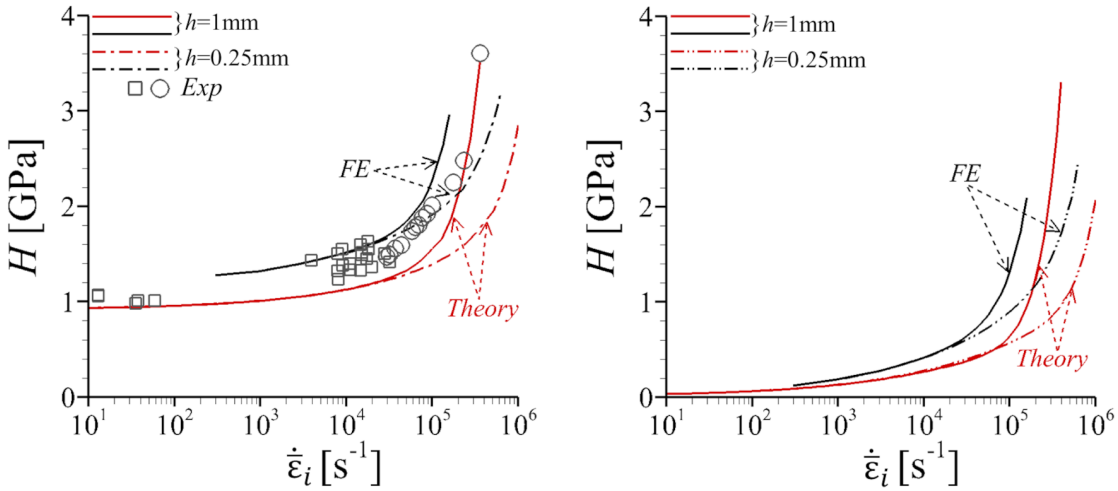

Figure 9: Comparison of the variation of hardness (H) with indentation strain-rate ($\dot{\bar{\varepsilon}}_i$) obtained from the finite element (FE) calculations and the analytical (Theory) model at two values of the indentation depth (h) and for a wide range of values of the imposed indentation velocity ($\dot{h}_0$). (a) For overstress power-law description for the strain-rate dependence. (b) For simple power-law description for the strain-rate dependence. The horizontal axis in both (a) and (b) are on the log scale. The experimental (Exp) results with square symbols in (a) are the uniaxial stress data of Rittel et al. (2002) converted to H with a Tabor factor of 3 and the strain-rate is the nominal uniaxial strain-rate, while those with circles are the indentation force - depth data of Lu et al. (2003) converted to H and $\dot{\bar{\varepsilon}}_i$ as per Eq. (8).

available experimental data for this material from the works of Rittel et al. (2002) and Lu et al. (2003) are also included in Fig. 9(a) for direct comparison.

As can be seen in Fig. 9, the analytical model and finite element results show the same dependence of H on $\dot{\bar{\varepsilon}}_i$ for both viscoplastic constitutive models. The analytical model predicts, like the finite element calculations, that at any given value of $\dot{\bar{\varepsilon}}_i < 5 \times 10^4$ s^{-1} (referred to as critical strain-rate in Section 3) the hardness is independent of the indentation depth. Similarly, for any given value of $\dot{\bar{\varepsilon}}_i > 5 \times 10^4$ s^{-1}, the analytical model predicts, in agreement with the finite element results, that the value of H depends on the indentation depth, with higher values obtained at greater depths, and increases rather rapidly with further increase in $\dot{\bar{\varepsilon}}_i$.

The limited experimental data for OFHC copper in Fig. 9(a) further confirms the rapid increase in the value of H with increasing $\dot{\bar{\varepsilon}}_i$ above a critical value of approximately 5×10^4 s^{-1}, as predicted by both the finite element calculations and the analytical model. However, the lack of hardness measurements at different indentation depths for a fixed value of the indentation strain rate does not capture the dependence of material hardness on indentation depth within these limited experimental results. The exact value of the critical indentation strain rate, $\approx 5 \times 10^4$ s^{-1}, obtained from the finite element calculations and analytical model, as well as observed in the experiments for OFHC copper subjected to dynamic indentation

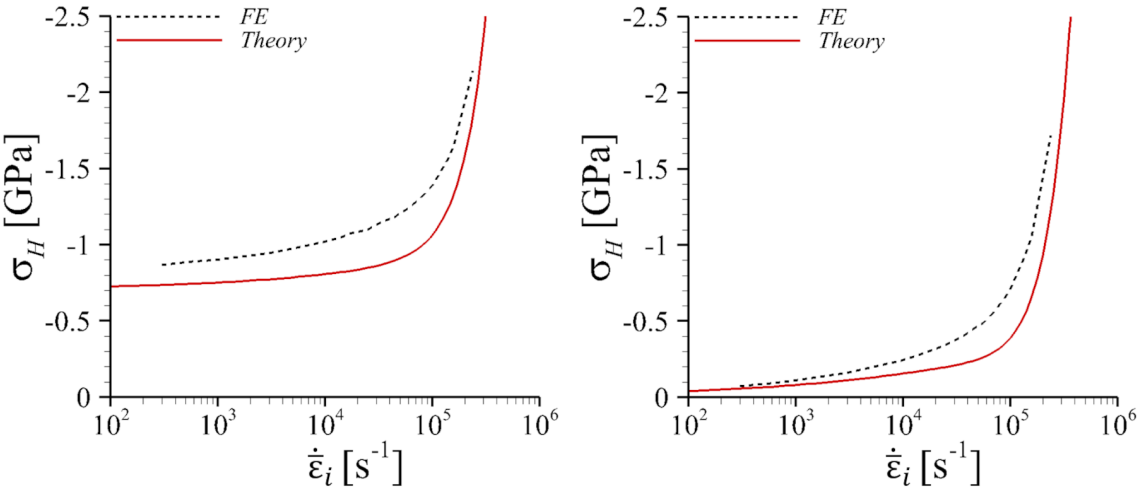

Figure 10: Comparison of the variation of hydrostatic stress (σ_H) with indentation strain-rate ($\dot{\bar{\varepsilon}}_i$) obtained from the finite element (FE) calculations and the analytical (Theory) model at a depth of 1 mm below the indenter tip for an indentation depth of $h = 1$ mm and for a wide range of values of the imposed indentation velocity ($\dot{h}_0$). (a) For overstress power-law description for the strain-rate dependence. (b) For simple power-law description for the strain-rate dependence. The horizontal axis in both (a) and (b) are on the log scale.

using a rigid conical indenter of fixed geometry, is likely to be influenced by both material and geometrical factors.

The rapid increase in material hardness (greater than what is expected based on the strain-rate dependent constitutive description) above a critical indentation strain-rate is due to the inertia-induced rapid increase in the hydrostatic stress (σ_H). The rapid increase in σ_H with $\dot{\bar{\varepsilon}}_i$ above a critical value of $\dot{\bar{\varepsilon}}_i$ is predicted by both the analytical model and the finite element calculations for both constitutive models, as shown in Fig. 10. For values of $\dot{\bar{\varepsilon}}_i$ below the critical value, inertia effects are negligible, and the increase in hydrostatic stress is proportional to the strain-rate dependent increase in the material's flow strength. However, for values of $\dot{\bar{\varepsilon}}_i$ above the critical value, inertia effects dominate, and the increase in hydrostatic stress is significantly greater than the expected increase due to the strain-rate dependent increase in the material's flow strength. Moreover, for $\dot{\bar{\varepsilon}}_i$ greater than the critical value, the relative contributions of inertia and strain-rate hardening to the development of the hydrostatic stress field are similar for both overstress and simple power-law models (for the range of indentation velocities considered in this work).

A similar rapid increase in the value of H with increasing $\dot{\bar{\varepsilon}}_i$ above a critical value of $\dot{\bar{\varepsilon}}_i$ has been observed, even for materials that follow a strain-rate independent constitutive description (dos Santos et al., 2021). For strain-rate independent materials, the rapid increase in H above a critical value of $\dot{\bar{\varepsilon}}_i$ was also attributed to the inertia-induced rapid increase in hydrostatic stress. This phenomenon, where inertia-induced hydrostatic stress becomes in-

creasingly significant above a certain loading-rate, is not unique to dynamic indentation and has been observed in various other dynamic problems. Examples of such problems include the formation of multiple necks in metal rings and shells subjected to rapid radial expansion (Rodríguez-Martínez et al., 2013, 2017), the competition between necking and fracture in porous ductile materials under dynamic loading (Zheng et al., 2020), and the collapse of voids in porous ductile materials subjected to shock loading (Lovinger et al., 2021), to name a few.

Although the analytical dynamic cavity expansion model and finite element calculation results are qualitatively consistent in Figs. 9 and 10, there are quantitative differences. Specifically, the finite element calculations consistently yield higher values of H (and σ_H) compared to the analytical model. The reasons for this quantitative discrepancy are not entirely clear but may be attributed to the simplifications made in the analytical dynamic cavity expansion model, such as the assumption of a spherically symmetric mechanical field and the absence of deviatoric stress within the hemispherical core representing the expanding cavity. Consequently, the simple analytical model cannot fully replace the necessity of finite element calculations when evaluating a material's response under dynamic indentation. Nevertheless, our results demonstrate that the simple analytical model accurately captures the fundamental physics of the dynamic indentation process and provides physically sound trends and results. Therefore, it can be employed in future works for promptly interpreting experimental results, identifying the underlying viscoplastic constitutive model of the material, and narrowing down the regions in the parameter space that merit further exploration.

In summary, the results presented here clearly demonstrate that the dependence of a material's hardness on indentation strain-rate below a critical value can be used to characterize the material's strain-rate sensitivity, provided the hardness vs. indentation strain-rate data are analyzed using a relation consistent with the underlying viscoplastic constitutive description of the material. Furthermore, the results also show that above the critical indentation strain-rate, the measured hardness is no longer characteristic of the material; instead, it is determined by the rapid increase in hydrostatic stress induced by inertia. As a consequence, any analysis of the material's hardness dependence on indentation strain-rate above the critical value will result in an apparent strain-rate sensitivity exponent that is greater than the inherent strain-rate sensitivity of the material. Moreover, above the critical indentation strain-rate, the indentation depth emerges as a natural length-scale that affects the measured hardness. This emergence of indentation depth as a length-scale is attributed to the inertial effects since the constitutive description of the material does not have an explicit length-scale. The significance of this length-scale is physically sound, as a deeper indentation requires more material displacement, leading to a stronger inertial effect and yielding higher hardness values. These findings were not only obtained from the results of extensive finite element analyses but also using a simple analytical dynamic cavity expansion model. Both the finite element method and the analytical model employed in this study rely on well-established theories and numerical tools, further ensuring the validity of these findings. Lastly, to the best of the authors' knowledge, this is the first-ever demonstration that inertia effects make dynamic hardness size-dependent and emphasizes the limitations

of using high-rate indentation tests to characterize the strain-rate sensitivity or strain-rate dependent flow strength of materials at high strain rates.

6. Concluding Remarks

This work focuses on two fundamental questions related to the dynamic indentation response of ductile materials: (i) Does the scaling of dynamic hardness with indentation strain-rate follow the same scaling as the strain-rate dependent constitutive description of materials? (ii) How does the interplay of materials' strain-rate dependence and the effects of inertia affect the scaling of dynamic hardness with indentation strain-rate? To answer these questions, we extensively analyzed the dynamic indentation response of ductile materials when indented using a rigid conical indenter over a wide range of indentation velocities. The materials are assumed to follow isotropic elastic-viscoplastic constitutive relations, with the viscoplastic part described by either an overstress or a simple power-law model. The dynamic indentation problem is solved computationally using both the finite element method and an analytical cavity expansion model. The predictions of the overstress power-law constitutive model were also validated using limited available experimental results for OFHC copper.

The key conclusions are as follows:

- Below a critical indentation strain-rate, the scaling of dynamic hardness with indentation strain-rate follows the constitutive model for both overstress and simple power-law models. Thus, allowing for the characterization of the material's strain-rate sensitivity, provided the hardness vs. indentation strain-rate data are analyzed using a relation consistent with the underlying constitutive description of the material.

- Above the critical indentation strain-rate, the dynamic hardness increases rather rapidly with increasing indentation strain-rate for both overstress and simple power-law models. This indicates that above the critical indentation strain-rate, dynamic hardness is no longer an intrinsic material property.

- The rapid increase in dynamic hardness with indentation strain-rate above the critical indentation strain-rate is due to the inertia-induced rapid increase in the hydrostatic stress in the specimen.

- Despite the absence of an explicit length-scale in materials' constitutive description, above the critical indentation strain-rate, the indentation depth emerges as a length-scale, resulting in higher dynamic hardness at greater depths. This is due to the increase in inertial effects resulting from the larger volume of material that needs to be displaced for deeper indentations.

In this work, we have addressed two fundamental questions associated with the dynamic indentation response of ductile materials. These two questions are extremely important since, to the best of the authors' knowledge, all prior works not only analyzed the dependence of dynamic hardness on indentation strain-rate assuming a simple power-law scaling between

the two but also neglected any potential influence of inertia. Additionally, to the best of the authors' knowledge, this paper presents the first-ever demonstration that inertia effects make dynamic hardness size-dependent and emphasizes the limitations in using high-rate indentation tests to characterize the strain-rate sensitivity or strain-rate-dependent flow strength of materials at high strain-rates.

All these conclusions were not only drawn from the results of extensive finite element analyses but were also verified using a simple analytical dynamic cavity expansion model. Both the finite element method and the analytical model employed in this study rely on well-established theories and numerical tools, further ensuring the validity of these conclusions. Moreover, the analytical dynamic cavity expansion model presented in this work effectively captures the fundamental physics of the dynamic indentation process and yields trends consistent with the full field finite element results. Thus, it can be utilized in future works for quick interpretation of experimental results, identification of the material's constitutive model, and narrowing down the regions in the parameter space that require further investigation.

Although in this work, we focused on the dynamic indentation of ductile materials characterized by two viscoplastic constitutive descriptions and used a rigid conical indenter of fixed geometry, the conclusions drawn here are likely applicable to a wide range of circumstances. However, we do note that some of the quantitative results, such as the value of the critical indentation strain-rate, will depend on both material and geometric parameters, such as material density and indenter geometry. Furthermore, investigating the dynamic indentation response of materials that follow pressure-dependent constitutive responses will be of great interest. This analysis will enable us to examine the effect of plastic compressibility on dynamic hardness measurements, particularly at higher indentation strain-rates where hydrostatic stress controls the dynamic hardness measurements. We hope that our work will inspire further research in these areas.

Acknowledgments

The finite element calculations reported on were carried out using high performance research computing resources provided by Texas A&M University.

Funding

This work was supported by the European Union's Horizon 2020 Programme (Excellent Science, Marie-Sklodowska-Curie Actions) under REA grant agreement 777896 (Project QUANTIFY); FAPERGS (Foundation for the Support of Research in the State of Rio Grande do Sul, Brazil), grant agreement 21/2551-0000744-3; and the U.S. National Science Foundation grant CMMI - 1944496.

Conflict of interest

The authors declare that they have no known competing financial interests or personal relationships that could have appeared to influence the work reported in this paper.

Author contributions

Zahra Ghasemi: Formal analysis; Investigation; Methodology; Software; Validation; Visualization; Writing - original draft. **Tiago dos Santos**: Formal analysis; Investigation; Funding acquisition; Methodology; Software; Validation; Visualization; Writing - review & editing. **José A. Rodríguez-Martínez**: Conceptualization; Formal analysis; Investigation; Funding acquisition; Methodology; Project administration; Supervision; Writing - original draft. **Ankit Srivastava**: Conceptualization; Data curation; Formal analysis; Funding acquisition; Methodology; Project administration; Supervision; Writing - original draft.

References

Batson, R., 1918. The value of the indentation method in the determination of hardness. Proceedings of the Institution of Mechanical Engineers 95, 463–483.

Belytschko, T., Chiapetta, R., Bartel, H., 1976. Efficient large scale non-linear transient analysis by finite elements. International Journal for Numerical Methods in Engineering 10, 579–596.

Bhattacharya, A., Nix, W., 1988. Finite element simulation of indentation experiments. International Journal of Solids and Structures 24, 881–891.

Calle, M., Mazzariol, L.M., Alves, M., 2018. Strain rate sensitivity assessment of metallic materials by mechanical indentation tests. Materials Science and Engineering: A 725, 274–282.

Chen, X., Ogasawara, N., Zhao, M., Chiba, N., 2007. On the uniqueness of measuring elastoplastic properties from indentation: the indistinguishable mystical materials. Journal of the Mechanics and Physics of Solids 55, 1618–1660.

Cohen, T., Durban, D., 2013a. Hypervelocity cavity expansion in porous elastoplastic solids. Journal of Applied Mechanics 80, 011017.

Cohen, T., Durban, D., 2013b. Plastic instabilities in porous cylinders under remote triaxial loading. European Journal of Mechanics - A/Solids 37, 193 – 199.

Cohen, T., Masri, R., Durban, D., 2010. Shock waves in dynamic cavity expansion. Journal of Applied Mechanics 77, 041009.

Cowper, G., Symonds, P., 1957. Strain hardening and strain rate effects in the impact loading of cantilever beams. Contract Report Tech. Report No. 28. Div. of Engng, Brown University. Providence, RI.

Crook, A., 1952. A study of some impacts between metal bodies by a piezo-electric method. Proceedings of the Royal Society of London. Series A. Mathematical and Physical Sciences 212, 377–390.

Danas, K., Deshpande, V., Fleck, N., 2012. Size effects in the conical indentation of an elasto-plastic solid. Journal of the Mechanics and Physics of Solids 60, 1605 – 1625.

Davies, R., 1949. The determination of static and dynamic yield stresses using a steel ball. Proceedings of the Royal Society of London. Series A. Mathematical and Physical Sciences 197, 416–432.

Davis, C., Hunter, S., 1960. Assessment of the strain-rate sensitivity of metals by indentation with conical indenters. Journal of the Mechanics and Physics of Solids 8, 235–254.

dos Santos, T., Brezolin, A., Rossi, R., Rodríguez-Martínez, J.A., 2020. Modeling dynamic spherical cavity expansion in elasto-viscoplastic media. Acta Mechanica 231, 2381–2397.

dos Santos, T., Srivastava, A., Rodríguez-Martínez, J.A., 2021. The combined effect of size, inertia and porosity on the indentation response of ductile materials. Mechanics of Materials 153, 103674.

Durban, D., Masri, R., 2004. Dynamic spherical cavity expansion in a pressure sensitive elastoplastic medium. International Journal of Solids and Structures 41, 5697–5716.

Fleck, N., Otoyo, H., Needleman, A., 1992. Indentation of porous solids. International Journal of Solids and Structures 29, 1613 – 1636.

Gao, X.L., Jing, X., Subhash, G., 2006. Two new expanding cavity models for indentation deformations of elastic strain-hardening materials. International Journal of Solids and Structures 43, 2193 – 2208.

Gray, G., 2000. Shock Wave Testing of Ductile Materials.. ASM International. pp. 530–538.
Guillonneau, G., Mieszala, M., Wehrs, J., Schwiedrzik, J., Grop, S., Frey, D., Philippe, L., Breguet, J.M., Michler, J., Wheeler, J.M., 2018. Nanomechanical testing at high strain rates: New instrumentation for nanoindentation and microcompression. Materials & Design 148, 39–48.
Hackett, B., Sudharshan Phani, P., Walker, C., Oliver, W., Pharr, G., 2023. Advances in the measurement of hardness at high strain rates by nanoindentation. Journal of Materials Research , 1–15.
Hassani, M., Veysset, D., Nelson, K.A., Schuh, C.A., 2020. Material hardness at strain rates beyond 10^6 s^{-1} via high velocity microparticle impact indentation. Scripta Materialia 177, 198–202.
Hopkinson, B., 1914. X. a method of measuring the pressure produced in the detonation of high, explosives or by the impact of bullets. Philosophical Transactions of the Royal Society of London. Series A, Containing Papers of a Mathematical or Physical Character 213, 437–456.
Hutchinson, J.W., Neale, K.W., 1977. Influence of strain-rate sensitivity on necking under uniaxial tension. Acta Metallurgica 25, 839–846.
Johnson, K., 1970. The correlation of indentation experiments. Journal of the Mechanics and Physics of Solids 18, 115 – 126.
Koeppel, B.J., Subhash, G., 1997. An experimental technique to investigate the dynamic indentation hardness of materials. Experimental Techniques 21, 16–18.
Kolsky, H., 1949. An investigation of the mechanical properties of materials at very high rates of loading. Proceedings of the physical society. Section B 62, 676.
Liu, Y., Fan, D., Bhat, S.P., Srivastava, A., 2020. Ductile fracture of dual-phase steel sheets under bending. International Journal of Plasticity 125, 80–96.
Liu, Y., Zheng, X., Osovski, S., Srivastava, A., 2019. On the micromechanism of inclusion driven ductile fracture and its implications on fracture toughness. Journal of the Mechanics and Physics of Solids 130, 21–34.
Liu, Z., Zhang, J., He, B., Zou, Y., 2021. High-speed nanoindentation mapping of a near-alpha titanium alloy made by additive manufacturing. Journal of Materials Research 36, 2223–2234.
Lovinger, Z., Czarnota, C., Ravindran, S., Molinari, A., Ravichandran, G., 2021. The role of micro-inertia on the shock structure in porous metals. Journal of the Mechanics and Physics of Solids 154, 104508.
Lu, J., Suresh, S., Ravichandran, G., 2003. Dynamic indentation for determining the strain rate sensitivity of metals. Journal of the Mechanics and Physics of Solids 51, 1923–1938.
Masri, R., Durban, D., 2005. Dynamic spherical cavity expansion in an elastoplastic compressible mises solid. Journal of applied mechanics 72, 887–898.
Mata, M., Casals, O., Alcalá, J., 2006. The plastic zone size in indentation experiments: The analogy with the expansion of a spherical cavity. International Journal of Solids and Structures 43, 5994 – 6013.
Merle, B., Higgins, W.H., Pharr, G.M., 2020. Extending the range of constant strain rate nanoindentation testing. Journal of Materials Research 35, 343–352.
Meyers, M.A., 1994. Dynamic behavior of materials. John wiley & sons.
Mok, C.H., Duffy, J., 1965. The dynamic stress-strain relation of metals as determined from impact tests with a hard ball. International Journal of Mechanical Sciences 7, 355–371.
Needleman, A., 2018. Effect of size on necking of dynamically loaded notched bars. Mechanics of Materials 116, 180–188. IUTAM Symposium on Dynamic Instabilities in Solids.
Nobre, J., Dias, A., Gras, R., 1997. Resistance of a ductile steel surface to spherical normal impact indentation: use of a pendulum machine. Wear 211, 226–236.
N'souglo, K.E., Srivastava, A., Osovski, S., Rodríguez-Martínez, J.A., 2018. Random distributions of initial porosity trigger regular necking patterns at high strain rates. Proceedings. Mathematical, physical, and engineering sciences 474 2211, 20170575.
Osovski, S., Srivastava, A., Bouchaud, E., Ravi-Chandar, K., Needleman, A., 2015. The effect of loading rate on ductile fracture toughness and fracture surface roughness. Journal of the Mechanics and Physics of Solids 76, 20–46.
Peirce, D., Shih, C.F., Needleman, A., 1984. A tangent modulus method for rate dependent solids. Computers & structures 18, 875–887.

Phani, P.S., Hackett, B., Walker, C., Oliver, W., Pharr, G., 2023. On the measurement of hardness at high strain rates by nanoindentation impact testing. Journal of the Mechanics and Physics of Solids 170, 105105.

Qin, L., Li, H., Shi, X., Beake, B.D., Xiao, L., Smith, J.F., Sun, Z., Chen, J., 2019. Investigation on dynamic hardness and high strain rate indentation size effects in aluminium (110) using nano-impact. Mechanics of Materials 133, 55–62.

Ramesh, K.T., 2008. High Rates and Impact Experiments. Springer US, Boston, MA. pp. 929–960.

Rittel, D., Ravichandran, G., Lee, S., 2002. Large strain constitutive behavior of OFHC copper over a wide range of strain rates using the shear compression specimen. Mechanics of Materials 34, 627–642.

Rodríguez-Martínez, J.A., Molinari, A., Zaera, R., Vadillo, G., Fernández-Sáez, J., 2017. The critical neck spacing in ductile plates subjected to dynamic biaxial loading: on the interplay between loading path and inertia effects. International journal of solids and structures 108, 74–84.

Rodríguez-Martínez, J.A., Vadillo, G., Fernández-Sáez, J., Molinari, A., 2013. Identification of the critical wavelength responsible for the fragmentation of ductile rings expanding at very high strain rates. Journal of the Mechanics and Physics of Solids 61, 1357–1376.

Rueda-Ruiz, M., Beake, B.D., Molina-Aldareguia, J.M., 2020. New instrumentation and analysis methodology for nano-impact testing. Materials & Design 192, 108715.

Schmalbach, K.M., Lin, A.C., Bufford, D.C., Wang, C., Sun, C.C., Mara, N.A., 2021. Nanomechanical mapping and strain rate sensitivity of microcrystalline cellulose. Journal of Materials Research 36, 2251–2265.

Shore, A., 1907. An instrument for testing hardness. Am. Mach 30, 747–751.

Studman, C.J., Moore, M.A., Jones, S.E., 1977. On the correlation of indentation experiments. Journal of Physics D: Applied Physics 10, 949–956.

Subhash, G., Koeppel, B.J., Chandra, A., 1999. Dynamic indentation hardness and rate sensitivity in metals. Journal of Engineering Materials and Technology 121, 257–263.

Sudharshan Phani, P., Oliver, W.C., 2017. Ultra high strain rate nanoindentation testing. Materials 10, 663.

Tabor, D., 1948. A simple theory of static and dynamic hardness. Proceedings of the Royal Society of London. Series A. Mathematical and Physical Sciences 192, 247–274.

Tanner, A.B., McDowell, D.L., 1999. Deformation, temperature and strain rate sequence experiments on OFHC Cu. International Journal of Plasticity 15, 375–399.

Taylor, G., 1946. James forrest lecture 1946. the testing of materials at high rates of loading. Journal of the Institution of Civil Engineers 26, 486–519.

Tirupataiah, Y., Sundararajan, G., 1991. A dynamic indentation technique for the characterization of the high strain rate plastic flow behaviour of ductile metals and alloys. Journal of the Mechanics and Physics of Solids 39, 243–271.

Tong, W., Clifton, R.J., Huang, S., 1992. Pressure-shear impact investigation of strain rate history effects in oxygen-free high-conductivity copper. Journal of the Mechanics and Physics of Solids 40, 1251–1294.

Yoshioka, M., Yoshioka, N., 1995. Dynamic process of vickers indentation made on glass surfaces. Journal of Applied Physics 78, 3431–3437.

Zehnder, C., Peltzer, J.N., Gibson, J.S.L., Korte-Kerzel, S., 2018. High strain rate testing at the nano-scale: A proposed methodology for impact nanoindentation. Materials & Design 151, 17–28.

Zheng, X., N'souglo, K.E., Rodríguez-Martínez, J.A., Srivastava, A., 2020. Dynamics of Necking and Fracture in Ductile Porous Materials. Journal of Applied Mechanics 87.